Journal Pre-proof

A thick bondline beam model for the adhesively bonded 3-point bending specimen

A.B. de Morais

Please cite this article as: de Morais AB, A thick bondline beam model for the adhesively bonded 3-point bending specimen, *International Journal of Adhesion and Adhesives*, https://doi.org/10.1016/j.ijadhadh.2019.102465.

This is a PDF file of an article that has undergone enhancements after acceptance, such as the addition of a cover page and metadata, and formatting for readability, but it is not yet the definitive version of record. This version will undergo additional copyediting, typesetting and review before it is published in its final form, but we are providing this version to give early visibility of the article. Please note that, during the production process, errors may be discovered which could affect the content, and all legal disclaimers that apply to the journal pertain.

A thick bondline beam model for the adhesively bonded 3-point bending specimen

A. B. de Morais

University of Aveiro, Department of Mechanical Engineering, RISCO research unit, Campus Santiago, 3810-193 Aveiro, Portugal, Tel.: +351 234 370830; fax: +351 234 370953; E-mail: abm@ua.pt

Abstract

The adhesively bonded 3-point bending specimen has been recently considered for evaluating the adhesive shear stress-strain behaviour. Its main advantage is avoiding the spurious end effects typical of lap-joints. A previous beam model proved to be fairly accurate for thin bondlines typical of structural joints. The present study extends such model to thick bondlines and achieves improved shear strain results. Model predictions were in very good agreement with finite element analyses of specimens with metal adherends and adhesive elastic-perfectly plastic behaviour. The present model will facilitate the inverse method needed to evaluate the parameters of a piecewise linear approximation to the adhesive shear stress-strain curve. Furthermore, two simplified models were shown to provide useful bounds for the shear stress-strain curve using only the basic load-displacement data.

Keywords: B. Steels; C. Stress analysis; D. Mechanical properties of adhesives; Three-point bending; Shear test.

1. Introduction

The adhesive behaviour under shear stresses is an essential input for the design of adhesive joints [1,2]. However, despite the several tests developed, measuring the adhesive shear stress-strain τ_a-γ_a curve is far from straightforward [3]. The thick-

1

adherend shear test (TAST), currently standardized by ASTM and ISO, has been the most widely used because of the relatively simple specimen and loading mode.

One of the main difficulties in adhesive shear tests is to measure γ_a, given the typical thin bondlines adopted in structural joints [3]. Special extensometers were thus developed for the aforementioned standard tests. However, measurement points are located in the adherends, thereby demanding corrections for adherend deformations. The increasing use of the digital image correlation (DIC) technique [4] seems to be a valid alternative to the special extensometers [5,6]. Nevertheless, some difficulties with noise and the need of corrections for adherend deformations remain [5,6].

The DIC measurements of [6] show another major problem in adhesive shear testing: the γ_a-distribution along the overlap of the TAST specimen has peaks at the joint ends. Strength measurements are thus affected by the typical joint end features i.e. adherend chamfers, rounded corners and spew fillets [7,8].

The relatively small bonded area used in the TAST and in other specimens [3] also raises the question of the representativeness of measured adhesive properties. Evidently, this question is particularly relevant for the substantially different approach of testing bulk specimens, given the special specimen manufacturing techniques needed.

Finally, the adhesively bonded 3-point bending (AB3PB) specimen (Fig. 1) has been recently considered a possible alternative to measure adhesive shear properties [9,10]. In fact, the specimen addresses one of the main problems identified above, as failure will initiate inside the bonded area, rather than at the joint ends [10]. Significantly large regions of nearly constant τ_a can also be achieved, thereby favouring the representativeness of results [10]. However, the AB3PB specimen will usually require thick high strength metal adherends in order to avoid adherend yielding.

Moreover, elastic-plastic analyses are needed for obtaining approximate τ_a-γ_a curves

through an inverse method that may require bondline strain measurements [10]. A beam

model was developed in [10] for obtaining an elastic-perfectly plastic approximation to

the τ_a-γ_a curve from relatively long specimens with typical 0.1-0.4 mm thick bondlines.

Compared to finite element analyses (FEA), the beam model of [10] gave accurate

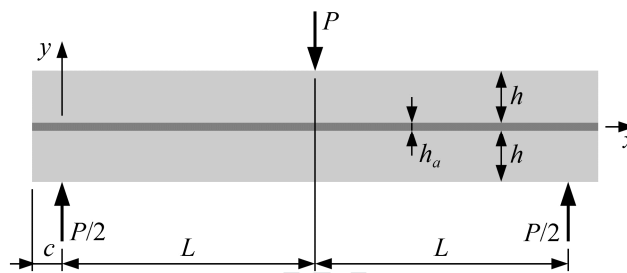strengths τ_{ua}, but underpredicted γ_a, with errors that could reach 17%.

Fig. 1. The adhesively bonded 3-point bending (AB3PB) specimen.

The present work extends the beam model of [10] to thick bondlines i.e. results

are here presented for bondlines up to 3 mm thick. In fact, such thick bondlines are

common in wind turbine blades [11], and are currently being considered for civil

engineering applications [12]. Ideally, adhesive shear properties should not depend on

the bondline thickness. However, studies with the napkin-ring [13,14] and TAST [15]

showed that the bondline thickness affects the shear strength and the failure strain.

According to Chai [13,14], the strong bondline thickness effect on the failure strain is

associated to the constraints imposed by the stiff adherends and to the probability of

finding large flaws.

The present beam model also predicts more accurately γ_a than the one of [10].

Furthermore, two simplified models derived provide bounds for the τ_a-γ_a curve just from

the basic load-displacement data. These developments facilitate considerably data

3

reduction, which requires an inverse method that evaluates the parameters of a τ_a-γ_a

curve base description.

2. The beam model

2.1. Fundamental equations

As in [10], one begins by analysing an infinitesimal element of the upper adherend (Figs.

1 and 2) at a distance $0 < x < L$ from the left support. The element cross-sections are

subjected to the normal force N, the transverse shear force V, the bending moment M.

The adhesive shear stress τ_a acts on the element lower surface. Two of the main

assumptions of [10] are here retained:

- neglect other adhesive stresses than τ_a, despite inevitable compression in the
  vicinity of supports and load-point;
- uniform τ_a across the bondline thickness.

Both assumptions proved to be accurate for the thin $h_a = 0.1$-0.4 mm bondlines

considered in [10], but, evidently, their suitability for thicker bondlines warranted
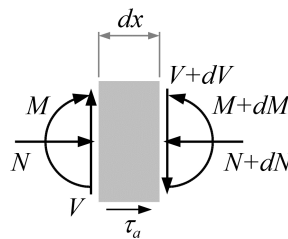
evaluation.

Fig. 2. Forces acting on an infinitesimal element of an AB3PB specimen upper adherend [10].

In this framework, the horizontal force, vertical force and moment equilibrium

equations of the adherend element are

$$\tau_a = \frac{1}{b}\frac{dN}{dx} \tag{1}$$

$$V = \frac{P}{4} - \frac{bh_a\tau_a}{2} \tag{2}$$

$$V = \frac{dM}{dx} + \frac{bh\tau_a}{2} \tag{3}$$

respectively, where b is the specimen width and h is the adherend thickness (Fig.1).

The present model also adopts initially Euler-Bernoulli beam theory,

$$M = EI\frac{d^2 v_b}{dx^2} \tag{4}$$

where E is the adherend Young's modulus, $I = bh^3/12$ is the adherend second moment of area and v_b is the beam bending vertical displacement. In fact, metal AB3PB specimens have high span-to-thickness (L/h) ratios, thus allowing a posteriori inclusion of the small transverse shear contribution. Combination of Eqs. (1)-(4) gives

$$\frac{d^3 v_b}{dx^3} = \frac{3[P - 2b(h + h_a)\tau_a]}{Ebh^3} \tag{5}$$

Where the kinematics is concerned, γ_a is associated with the longitudinal adherend relative displacement u_a. The latter is generated by the bending rotations, which can be taken as dv_b/dx in the geometrically linear regime, and by axial strains (Fig. 3). As in [10], uniform bondline through-thickness γ_a is assumed. However, instead of the $\gamma_a = u_a/h_a$ thin bondline hypothesis adopted in [10], the rotation term is now included i.e.

$$\gamma_a = \frac{u_a}{h_a} - \frac{dv_b}{dx} \tag{6}$$

an expression that bears the $\gamma_a \geq 0$, $u_a \geq 0$ and $dv_b/dx \leq 0$ sign conventions. In particular, because of the symmetry about the $x = L$ plane of the specimen (Fig. 1), $(dv_b/dx)_{x=L} = 0$ and $u_a(L) = 0$, and so we have

$$h_a\gamma_a = -(h + h_a)\frac{dv_b}{dx} - 2\int_x^L \frac{N}{Ebh}dx \tag{7}$$

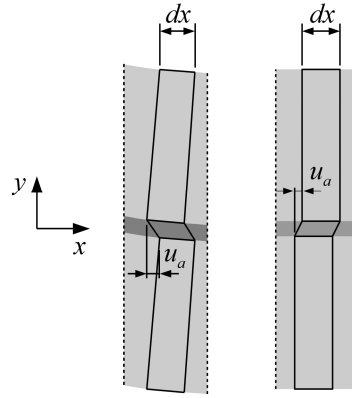using the $N \geq 0$ sign convention.

Fig. 3. Contributions of the bending rotations (left) and axial strains (right) to the bondline shear strains.

It is worth noting that all of the above equations apply to the $-c \leq x \leq 0$ overhung region by letting $P = 0$. The analysis of the overhang is identical to the one of [10], and thus is not detailed here. Again, as done in [10], the adhesive behaviour herein adopted is elastic-perfectly plastic (Fig. 4) for model evaluation purposes.
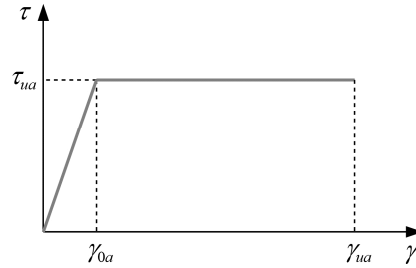

Fig. 4. Pure shear elastic-perfectly plastic behaviour adopted for the adhesive.

2.2. Solution procedures

The solution for the initial loading stages in which the adhesive remains linear elastic starts by substituting τ_a/G_a for γ_a in Eq. (7), G_a being the adhesive shear modulus, performing a double differentiation, and substituting Eq. (1) for dN/dx. This leads to a 2nd order differential equation for τ_a whose solution can be written as

$$\tau_a = \tau_R + \tau_0 e^{-\lambda x} + \tau_1 e^{\lambda x} \tag{8}$$

where τ_0 and τ_1 are integration constants,

$$\lambda = \sqrt{\frac{G_a[2h^2+6(h+h_a)^2]}{Eh^3h_a}} \qquad (9)$$

is the elastic shear stress distribution parameter and

$$\tau_R = \frac{3(h+h_a)P}{b[2h^2+6(h+h_a)^2]} \qquad (10)$$

is the limit "remote" shear stress i.e. the maximum τ_a that can act in the regions

sufficiently distant from the support and load-point (Fig. 1). In fact, by letting $h_a = 0$ i.e.

for a homogeneous $2h$-thick beam under 3PB, Eq. (10) becomes equal to the well-

known mechanics of materials $3P/8bh$ maximum transverse shear stress.

The next stage is substituting Eq. (8) for τ_a in Eq. (5), which is then successively

integrated until v_b, thereby introducing new integration constants. Eq. (8) is also to be

substituted for τ_a in Eq. (1), which is afterwards integrated for N. All integration

constants are obtained by the specimen boundary conditions and the τ_a, N, M, dv_b/dx and

v_b continuity conditions with the overhang. For the sake of conciseness and because of

the similarity with [10], the detailed derivation of the present model equations is not

done here. Nevertheless, the Appendix outlines briefly the procedures and conditions

employed in such derivations. Fig. 5 plots schematically the τ_a-distribution during the

elastic stage (0). It reaches the peak limited by τ_R near the $x = L/2$ and $x = 3L/2$ positions,

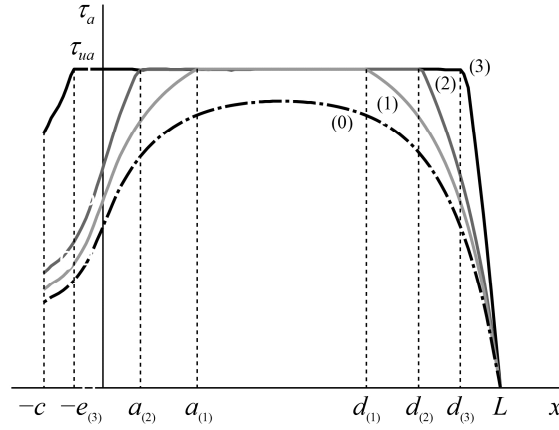while it decreases towards the overhang and $x = L$, where symmetry demands that $\tau_a = 0$.

Fig. 5. Schematic representation of the shear stress distribution along the bondline at 4 loading stages. The *a* or *e* left-end and *d* right-end limit coordinates of the plastic region are marked.

Evidently, at sufficiently high loads P, τ_{ua} is reached and an adhesive plastic zone is formed (Fig. 5). At higher loads, the plastic zone can encompass the entire overhang, but an elastic region always exists near $x = L$. As in the elastic case, equations for the plastic zone are derived by substituting τ_{ua} for τ_a in Eqs. (5) and (1), which are subsequently integrated for v_b and N, respectively. Integration constants for the elastic and plastic regions, as well as the limit coordinates of the plastic region (Fig. 5), are determined by the aforementioned boundary and continuity conditions, which are detailed in the Appendix. Specifically, before the plastic zone reaches the overhang, it can be shown that the limiting coordinates (Fig. 5) are obtained by solving the Eqs.

$$d = a + \frac{2\tau_R \eta_c + 2(\tau_{ua} - \tau_R)[\eta_c \cosh(\lambda a) - \sinh(\lambda a)]}{\lambda(\tau_{ua} - \tau_R)[\cosh(\lambda a) - \eta_c \sinh(\lambda a)]} \tag{11}$$

$$a - d = \frac{2(\tau_{ua} - \tau_R)\cosh(\lambda(L-d)) + 2\tau_R}{\lambda(\tau_{ua} - \tau_R)\sinh(\lambda(L-d))} \tag{12}$$

where

$$\eta_c = -\tanh(\lambda c) \tag{13}$$

is the overhang elastic factor. This requires no more than a simple one-variable

8

numerical iterative procedure e.g. the secant method [16] using a as the main variable, obtaining d from Eq. (11) and adopting Eq. (12) as error function.

For the partially plastic overhang, evaluation of e and d (Fig. 5) can be done by iterating on the former and computing, successively, the equivalent overhang distance

$$c_e = e + \frac{\tanh(\lambda(c-e))}{\lambda} \tag{14}$$

d from the well-known closed-form solution of the quadratic equation

$$(\tau_R - \tau_{ua})d^2 - (2c_e\tau_{ua})d - \tau_{ua}e(2c_e - e) = 0 \tag{15}$$

until

$$\frac{\lambda d \sinh(\lambda(L-d)) + \cosh(\lambda(L-d)) - 1}{\lambda(c_e + d)\sinh(\lambda(L-d)) + \cosh(\lambda(L-d))} = \frac{\tau_{ua}}{\tau_R} \tag{16}$$

At last, for fully plastic overhang (Figs. 1 and 5), d is obtained by solving Eq. (16) with $c_e = c$.

2.3. Main model outputs

In the initial elastic stage, τ_a along the main $0 \le x \le L$ region is given by Eq. (8) with

$$\frac{2\tau_0}{\tau_R} = \frac{\eta_c(e^{\lambda L} - 1) - 1}{\cosh(\lambda L) - \eta_c \sinh(\lambda L)}, \frac{2\tau_1}{\tau_R} = \frac{\eta_c(1 - e^{-\lambda L}) - 1}{\cosh(\lambda L) - \eta_c \sinh(\lambda L)} \tag{17}$$

and this stage ends when

$$\tau_{a,max} = \tau_R - 2\sqrt{\tau_0\tau_1} \tag{18}$$

reaches τ_{ua}. The beam bending load-point displacement is

$$\frac{EIv_b(L)}{b\tau_R} = -\frac{h^2 L^3}{18(h + h_a)} - \frac{h + h_a}{2\lambda^3}(\lambda L - \xi_e) \tag{19}$$

where

$$\xi_e = \frac{2\eta_c[1 - \cosh(\lambda L)] + \sinh(\lambda L)}{\cosh(\lambda L) - \eta_c \sinh(\lambda L)} \tag{20}$$

As mentioned above, the load-point displacement δ includes the contribution of

9

transverse shear, so that [10]

$$\delta = |v_b(L)| + \frac{3L(1-h_a/2h)}{10bhG} \tag{21}$$

G being the adherend shear modulus.

The next loading stage involves adhesive yielding with elastic overhang (Fig. 5). After evaluating the a and d coordinates from Eqs. (11) and (12), the γ_a-distributions in the $0 \le x \le a$, $a \le x \le d$ and $d \le x \le L$ regions are given by

$$\gamma_a(x) = \frac{\tau_R}{G_a} - \frac{\eta_c \tau_R \sinh(\lambda(x-a)) + (\tau_R - \tau_{ua})[\cosh(\lambda x) - \eta_c \sinh(\lambda x)]}{G_a[\cosh(\lambda a) - \eta_c \sinh(\lambda a)]} \tag{22}$$

$$\gamma_a(x) = \gamma_{0a} + \frac{\tau_R - \tau_{ua}}{2G_a}\lambda^2(x-a)(d-x) \tag{23}$$

$$\gamma_a(x) = \frac{\tau_R}{G_a} - \frac{\tau_R \sinh(\lambda(x-d)) + (\tau_R - \tau_{ua})\sinh(\lambda(L-x))}{G_a \sinh(\lambda(L-d))} \tag{24}$$

respectively, with maximum at $x = (a + d)/2$. The beam bending load-point displacement is now

$$\frac{EIv_b(L)}{b(h+h_a)} = -\left(\frac{h}{h+h_a}\right)^2 \frac{\tau_R L^3}{18} - \frac{\tau_R L}{2\lambda^2} - \frac{(\tau_R - \tau_{ua})(d-a)^3}{24} + \frac{\xi_d - \xi_a}{2\lambda^3} \tag{25}$$

with

$$\xi_a = \frac{(\tau_R - \tau_{ua})\sinh(\lambda a) + \eta_c \tau_{ua}[1 + \cosh(\lambda a)]}{\cosh(\lambda a) - \eta_c \sinh(\lambda a)} \tag{26}$$

$$\xi_d = (2\tau_R - \tau_{ua})\tanh\left[\frac{\lambda(L-d)}{2}\right] \tag{27}$$

while Eq. (21) gives the total load-point displacement.

When the overhang becomes partially plastic (Fig. 5), the e and d coordinates are computed by solving Eqs. (15) and (16). The γ_a-distribution along the $0 \le x \le d$ region is

$$\gamma_a(x) = \gamma_{0a} + \frac{\lambda^2(d-x)[(\tau_R - \tau_{ua})(d+x) - 2\tau_{ua}c_e]}{2G_a} \tag{28}$$

attaining the peak at $x = \tau_{ua}c_e/(\tau_R - \tau_{ua})$, whereas Eq. (24) still holds for the $d \le x \le L$ region. The bending component of load-point displacement can be written as

$$\frac{EIv_b(L)}{b(h+h_a)} = -\left(\frac{h}{h+h_a}\right)^2 \frac{\tau_R L^3}{18} - \frac{\tau_R L}{2\lambda^2} - \frac{(\tau_R - \tau_{ua})}{6}\left(d^3 - \frac{3d}{\lambda^2}\right) + \frac{\tau_{ua}c_e d^2}{4} + \frac{\xi_d}{2\lambda^3} \qquad (29)$$

Finally, Eqs. (28) and (29) can be used for the fully plastic overhang by letting c_e = c after obtaining d from Eq. (16).

As seen in [10], one of the limitations of the AB3PB specimen is the risk of adherend yielding before bondline failure, especially for ductile adhesives. The maximum M and N occur at $x = L$, generating the maximum adherend normal stress

$$\sigma_{max} = \frac{\tau_R(2h+h_a)L}{h(h+h_a)} + \frac{2h+3h_a}{\lambda h^2}\left[\frac{\tau_{ua}}{\sinh(\lambda(L-d))} + \tau_R \tanh\left(\frac{\lambda(L-d)}{2}\right)\right] \qquad (30)$$

It is thus clear that the present model retains the simplicity of the one of [10], enabling an easy spreadsheet implementation. Most of the equations are quite similar, but, as shown below, the modified kinematics expressed by Eqs. (6) and (7) improved significantly the accuracy of γ_a-distributions, allowing application to thick bondlines.

3. Model evaluation

As discussed in [10], AB3PB specimens need to have relatively large span-to-thickness ratios so that:

- spurious stress components do not play a relevant role, specially the thickness-wise compression stresses near the supports and load-point;

- considerable regions of nearly constant τ_a are generated;

- the specimen is not too stiff, enabling the bondline to reach the adhesive failure strain γ_{ua} (Fig. 4).

However, an excessive length may induce σ_{max} values (Eq. (30)) high enough to cause premature adherend yielding. Thick high strength steel adherends will usually be needed for measuring the τ_a-γ_a curve of typical ductile adhesives [10]. Accordingly, we consider

here:

- adherends with Young's modulus E = 210 GPa and Poisson's ratio v = 0.3;

- adhesives with E_a = 1.8 GPa and v_a = 0.35.

The specimen geometries herein adopted (Table 1) were selected so that:

- fairly high τ_{ua}= 40 MPa [15,17,18], γ_{ua}= 20% (Fig. 4) could be attained for 2-3 mm thick bondlines, while allowing γ_{ua}= 30 and 40% for h_a = 0.5 and 0.1 mm, respectively;

- σ_{max} < 1300 MPa, a value well within the reach of quench and tempered alloy steels [19].

Evidently, testing thicker bondlines demands thicker adherends and, consequently, longer specimens. Nevertheless, the selected specimens fit in the workspace of typical universal testing machines.

Table 1. Specimen geometries adopted in this study (Fig. 1) and respective λL parameter values. The specimen width was b = 20 mm.

h_a (mm)	h (mm)	L (mm)	c (mm)	λL
0.1	4	35	7	8.99
0.5	10	90	10	6.66
2.0	25	230	15	5.50
3.0	30	270	15	4.88

The present model is now compared with 2D finite element (FE) models similar to those of [10]. The models were constructed with the 8-node solid quadratic reduced integration elements of Abaqus®. Mesh refinement studies showed that accurate results could be obtained by modelling (see Table 1): the bondline with 1 (h_a = 0.1-0.5 mm) or 2 (h_a = 2.0-3.0 mm) layers of solids elements; each adherend with 2 (h = 4-10 mm) or 4

(h = 25-30 mm) layers of solids elements; lengthwise element sizes of 0.5 mm (h_a = 0.1-0.5 mm) or 1 mm (h_a = 2.0-3.0 mm). Given the beam-like geometry, plane stress was assumed for the adherends. In turn, the bondline was modelled with plane strain elements, due to the strong constraints imposed by the stiff adherends. Geometrically non-linear analyses were conducted assuming elastic adherends and elastic-plastic adhesive with von Mises yield behaviour. Owing to the $x = L$ symmetry plane (Fig. 1), only half-specimen was modelled.

Firstly, it was seen that the elastic τ_a-distributions agree very well with FE results (Fig. 6). The latter confirmed that τ_a was practically constant across the bondline thickness, even for the thickest h_a = 3.0 mm one. Values presented in Fig. 6 are actually thickness-wise averages normalized by τ_R at load values low enough for the adhesive to remain elastic. It should be noted that the aforementioned mesh refinement employed in FE models provided many more points than those plotted in Fig. 6. A selection of points was made just for clarity purposes.
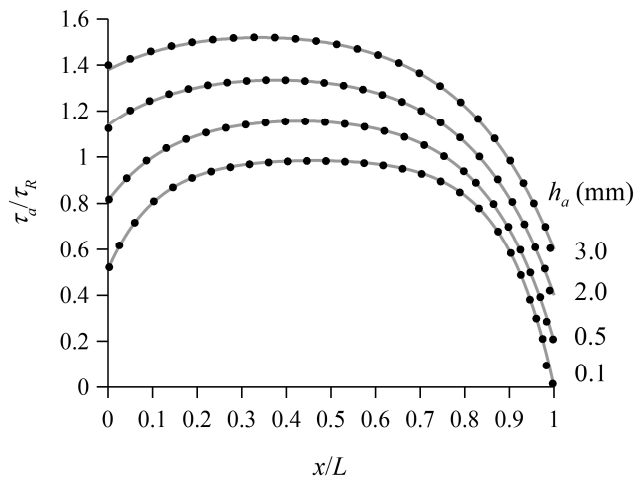

Fig. 6. Bondline normalized shear stress distributions predicted by the beam (grey lines) and FE (selected black points) models for the specimens of Table 1 under elastic conditions. For clarity, the curves for specimens with h_a = 0.5, 2.0 and 3.0 mm were vertically offset by 0.2, 0.4 and 0.6 units, respectively. Note that $\tau_a = 0$ at $x = L$.

Figs. 7-8 compare beam and FE model predictions for τ_R-δ/L curves, which are proportional to the common load-displacement P-δ ones. The improvements of the present beam model relative to the one of [10] were seen at the elastic stage. In fact, errors in initial specimen compliance were lower than 0.7%, even for the thickest $h_a =$ 3.0 mm bondline specimen, which had a low $\lambda L = 4.9$ (Table 1). In [10] errors reached 6.2% for specimens with $\lambda L = 7.5$, and thus $\lambda L \geq 9$ had been recommended. Specimens with low λL have some advantage in terms of increased sensitivity of the P-δ curve to the bondline properties. Nevertheless, λL needs to be high enough so that a region of nearly constant τ_a is achieved. It is worth noticing that Figs. 7-8 show that the specimen response is quite sensitive to τ_{ua}, despite the use of stiff adherends. This confirms that the AB3PB specimen is particularly well-suited for measuring τ_{ua}.
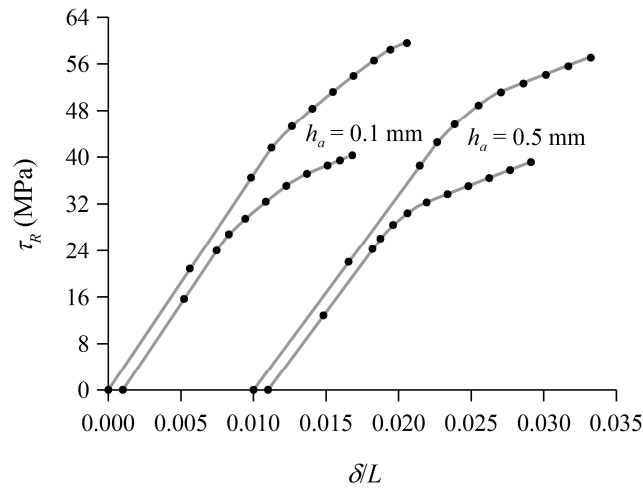

Fig. 7. Remote shear stress Eq. (10) versus normalised load-point displacement curves predicted by the beam (grey lines) and FE (selected black points) models for thin bondline specimens (see Table 1) with $\tau_{ua} =$ 25 and 40 MPa. For clarity, some curves were horizontally offset.
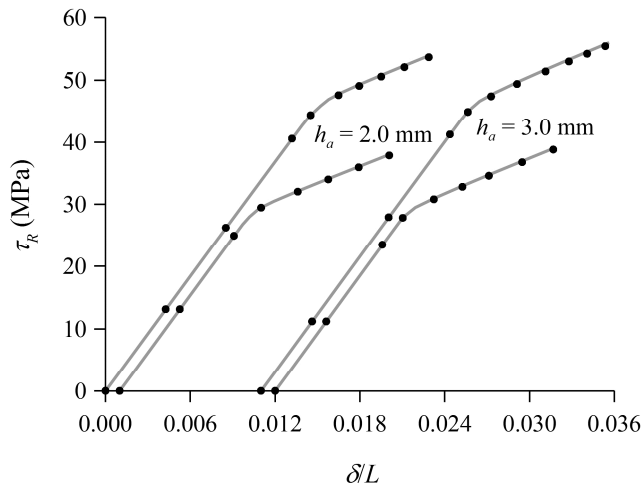
Fig. 8. Remote shear stress Eq. (10) versus normalised load-point displacement curves predicted by the

beam (grey lines) and FE (selected black points) models for thick bondline specimens (see Table 1) with

τ_{ua} = 25 and 40 MPa. For clarity, some curves were horizontally offset.

The main weakness of the model developed in [10] concerned γ_a-predictions.

When plotted against P, the maximum γ_a of FE results could be underestimated by 17%

during the adhesive plastic stages [10]. In an identical exercise, the underestimation of

the maximum γ_a was here lower than 3.5%. Moreover, if comparison with FE results is

made on the basis of identical specimen compliance $C = \delta/P$, the accuracy of the present

model was even better i.e. errors in the peak γ_a varied from −0.3% to 1.2% when h_a =

0.1-3.0 mm. In fact, as shown in Figs. 9-10, the present model predicted very well the

γ_a-distributions at the approximate maximum γ_a = 20-40% considered. Again, it is worth

remarking that FE results confirmed γ_a to be practically constant across the bondline

thickness. Values presented in Figs. 9-10 are, again, thickness-wise averages selected

from a vaster set of points available by the refined meshes adopted. Figs. 9-10 show

another interesting feature of the AB3PB specimen: it contains fairly long zones along

which γ_a is quite close to its maximum, especially for thick bondlines. This favours the
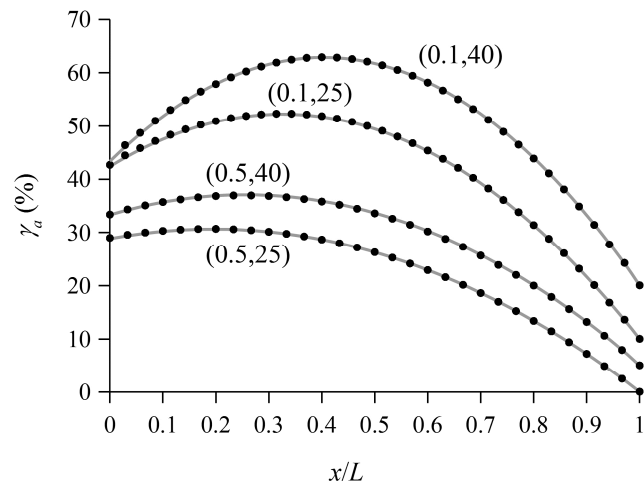
representativeness of experimental results.

Fig. 9. Bondline shear strain distributions predicted by the beam (grey lines) and FE (selected black points) models for specimens with the (h_a,τ_{ua}) values indicated (see Table 1). For clarity, some curves were vertically offset by 5-20%. Note that $\gamma_a = 0$ at $x = L$.

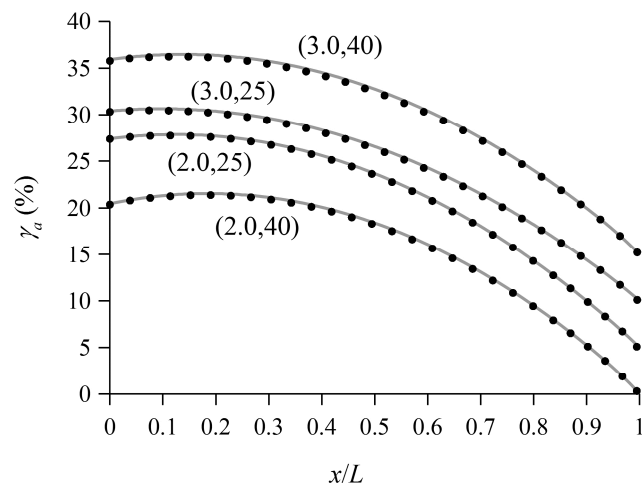Fig. 10. Bondline shear strain distributions predicted by the beam (grey lines) and FE (selected black points) models for specimens with the (h_a,τ_{ua}) values indicated (see Table 1). For clarity, some curves were vertically offset by 5-15%. Note that $\gamma_a = 0$ at $x = L$.

4. Data reduction methods

Having demonstrated the accuracy of the present beam model and illustrated some relevant characteristics of the AB3PB specimen, the issue is now model application in

16

experimental data reduction. Several approaches can be envisaged, but they all involve an inverse method i.e. evaluation of the parameters of a τ_a-γ_a curve base description.

The most obvious and simple approach consists of using the present model to fit the P-δ curve. The optimization problem is thereby reduced to the G_a and τ_{ua} parameters of the elastic-perfectly plastic approximation (Fig. 4). This approach is likely to provide accurate τ_{ua} for ductile adhesives, as they tend to present a plateau τ_a for a wide γ_a range. Moreover, as seen above, P-δ curves are quite sensitive to τ_{ua} (Figs. 7 and 8). However, owing to the limitations of the elastic-perfectly plastic approximation, a global fit to the P-δ curve will provide a secant modulus G_a, rather than the tangent modulus, which corresponds to the initial truly elastic region. In principle, one may attempt to evaluate the true G_a by applying the present beam model Eq. (19) to the initial part of the P-δ curve. The difficulty here resides on the low sensitivity of the latter to G_a, which is a side effect of the relatively high specimen stiffness needed to avoid premature adherend yielding. This limitation was already identified in [10] for thin bondlines and is confirmed by the present results for the specimens with h_a = 0.1 mm: a 20 % increase of G_a around the value adopted in the above simulations only results in a 1.6 % decrease of the initial compliance. Such decrease is more pronounced for specimens with thicker h_a = 2.0-3.0 mm bondlines i.e. 3.6-4.3 %, but remains somewhat modest.

In turn, the AB3PB lends itself to a far more elaborate approach involving simultaneously:

- a more accurate base τ_a-γ_a curve e.g. a piece-wise linear approximation that can be implemented in the beam model with closed-form expressions similar to the above ones;

- bondline γ_a-distributions measured by DIC [4].

17

Actually, a similar inverse method using FEA, DIC and the short beam specimen was applied to the shear behaviour of composites [20]. Besides involving a more complex mathematical optimization procedure, this approach may suffer from difficulties in DIC γ_a-measurements along the long bondlines of AB3PB specimens.

Regardless of the method employed, initial estimates of the τ_a-γ_a curve or of the parameters of the base approximation are welcome. Here we propose 2 bounds that can be derived from the above model, and easily applied in experimental data reduction. The upper bound, designated as pseudo-elastic, adopts elastic behaviour throughout the entire loading process. Therefore, for each (P,δ) point, one must successively:

- compute τ_R and v_b from Eqs. (10) and (21), respectively;

- solve Eq. (19) for λ by a simple iterative method e.g. Newton-Raphson; note that Eq. (9) provides G_a during the initial truly elastic stage, and a decreasing apparent G_a towards the failure point;

- obtain an estimated point of the τ_a-γ_a curve by letting $\tau_a = \tau_{a,max}$ of Eq. (18) and $\gamma_a = \tau_{a,max}/G_a$.

In turn, a lower bound for the τ_a-γ_a curve can be obtained from a constant stress model i.e. assuming that τ_a is constant along the bondline at each (P,δ) point. With this strong simplification, Eqs. (1)-(7) quick lead to

$$\tau_a = \frac{PL^3 - Ebh^3|v_b(L)|}{b(h+h_a)(2L+3c)L^2} \tag{31}$$

$$\gamma_a = \frac{[h^2 + 3(h+h_a)^2][L(\tau_R - \tau_a) - c\tau_a]^2}{Eh^3 h_a(\tau_R - \tau_a)} \tag{32}$$

the latter corresponding to the maximum shear strain along the bondline.

Figs. 11 and 12 show the application of such simplified models to the above FE simulations for the thickest and thinnest bondlines. As expected, the pseudo-elastic model predicted very accurately the elastic part of the elastic-perfectly plastic τ_a-γ_a

curve used in the simulations, but afterwards underestimated γ_a and overestimated τ_a. In turn, the constant stress model overestimated γ_a and underestimated τ_a, especially at the elastic stages, but became very accurate at sufficiently high plasticity levels. The simplified models gave broader bounds for the thinnest h_a= 0.1 mm bondline. This can be understood by looking at the steeper decrease of τ_a towards the overhang depicted in Fig. 6. Nevertheless, the results of Figs. 11 and 12 show the usefulness of the simplified models as a basis for obtaining the true τ_a-γ_a curve by more sophisticated approaches, such as the one outlined above.
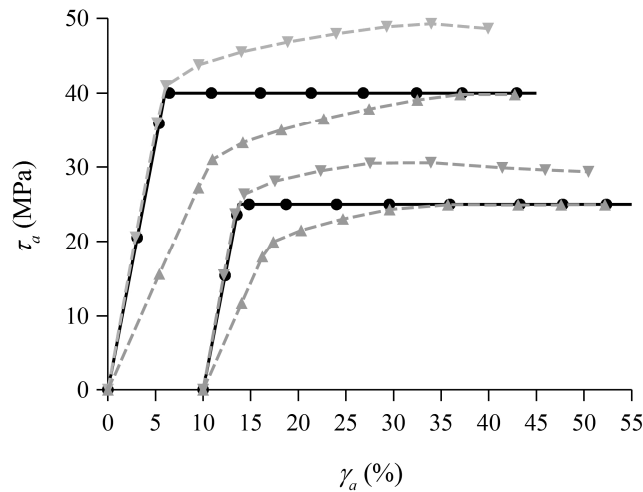

Fig. 11. Shear stress-strain curves estimated by the simplified pseudo-elastic (▼) and constant stress (▲) models from selected points of FE simulations (●) for h_a = 0.1 mm bondlines with elastic-perfectly plastic behaviour (black lines). For clarity, curves for τ_{ua} = 25 MPa were horizontally offset by 10%.

Fig. 12. Shear stress-strain curves estimated by the simplified pseudo-elastic (▼) and constant stress (▲) models from selected points of FE simulations (●) for h_a = 3.0 mm bondlines with elastic-perfectly plastic behaviour (black lines). For clarity, curves for τ_{ua} = 25 MPa were horizontally offset by 5%.
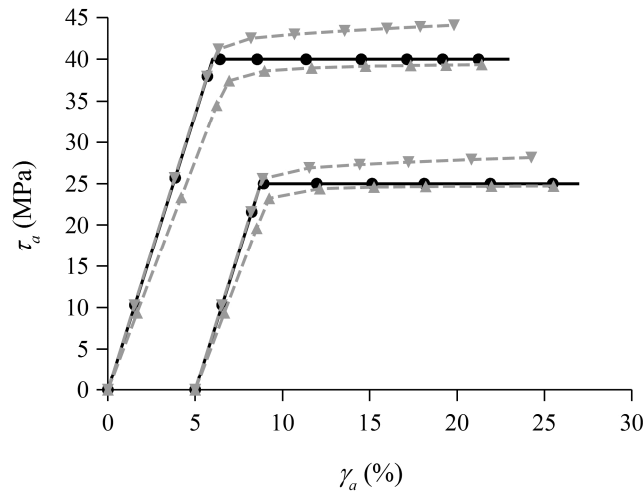
A final evaluation of the simplified models was made with FE simulations based on trilinear τ_a-γ_a model curves, characterized by a yield stress equal to $0.4\tau_{ua}$, a 2nd point of $\tau_a = 0.9\tau_{ua}$ and γ_a= 10%, and the failure point at γ_{ua}= 20%. First of all, τ_R-δ/L curves were compared with those of elastic-perfectly plasticity with identical G_a, τ_{ua} and γ_{ua} (Fig. 13). The sensitivity to the adhesive τ_a-γ_a curve was relatively low for very thin h_a = 0.1 mm bondlines. Nonetheless, the performance of the simplified models was similar to the elastic-perfectly plastic case (Figs. 14 and 15), providing tighter bounds for thick bondlines. The τ_a-overestimation of the pseudo-elastic model remained small during the first plastic hardening linear branch. Moreover, this model was quite sensitive to the beginning of the last plastic branch. From the practical viewpoint, the accuracy of constant stress model can be assessed from the initial differences relative to the pseudo-elastic model. Furthermore, the hardening predicted (Figs 14 and 15) gives another sign of τ_a-underestimation, as opposed to the plateaux reached for elastic-perfect plasticity (Figs. 11 and 12).
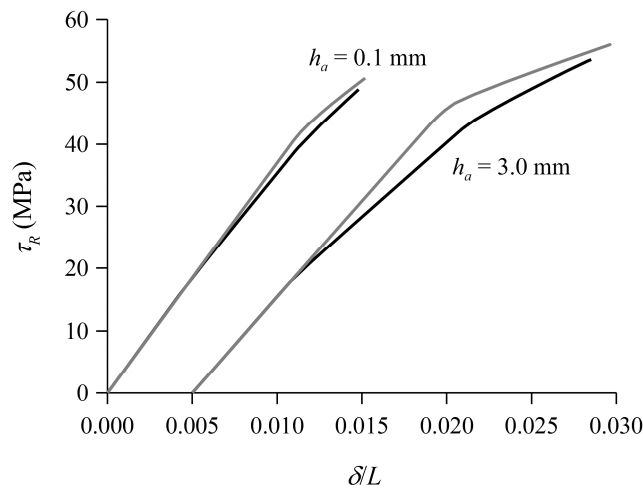
Fig. 13. Remote shear stress Eq. (10) versus normalised load-point displacement curves for elastic-perfectly plastic (grey lines) and trilinear (black lines) τ_a-γ_a curves models (see text and Table 1 for details). For clarity, curves for h_a = 3.0 mm were horizontally offset by 0.005 units.

Fig. 14. Shear stress-strain curves estimated by the simplified pseudo-elastic (▼) and constant stress (▲) models from selected points of FE simulations (black lines) for h_a = 0.1 mm bondlines with trilinear (●) τ_a-γ_a curve. For clarity, curves for τ_{ua} = 25 MPa were horizontally offset by 10%.
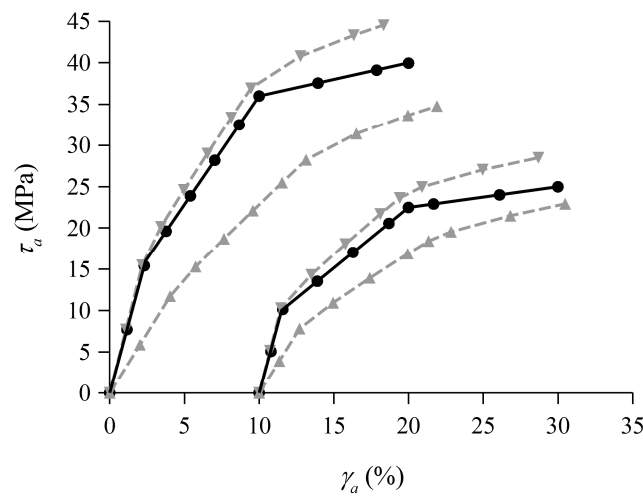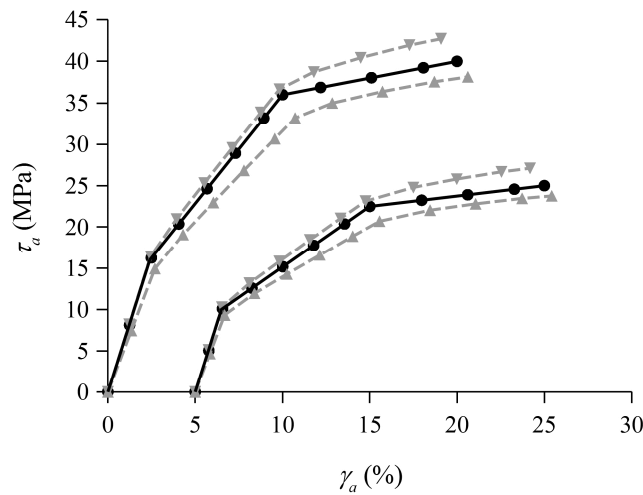
21

Fig. 15. Shear stress-strain curves estimated by the simplified pseudo-elastic ($\blacktriangledown$) and constant stress ($\blacktriangle$) models from selected points of FE simulations (black lines) for $h_a = 3.0$ mm bondlines with trilinear ($\bullet$) τ_a-γ_a curve. For clarity, curves for $\tau_{ua} = 25$ MPa were horizontally offset by 5%.

5. Concluding remarks

The improved beam model of the metal adhesively bonded 3-point bending (AB3PB) specimen here developed widens the perspectives for its usage to characterize the adhesive shear stress-strain behaviour. This results from the accurate shear strain distributions predicted and from the applicability to thick bondlines. One can apply the more basic data reduction approach which consists of deriving an elastic-perfectly plastic approximation from the load-displacement curve. Nevertheless, the beam model can be used in a more elaborate inverse method which optimizes the parameters of a piece-wise linear description of the adhesive shear stress-strain curve. In fact, such description can be easily implemented in the present beam model, leading to closed-form expressions similar to the ones obtained here for elastic-perfect plasticity. The beam model facilitates parameter optimization relative to finite element modelling. In any case, the inverse method is likely to demand bondline shear strain distributions measured by digital image correlation in order to yield accurate stress-strain curves.

22

Nevertheless, the beam model also enabled the derivation of simplified pseudo-elastic and constant stress models that provide bounds for the adhesive shear stress-strain curve just from the basic load-displacement data.

The present advances in data reduction add to the advantages of the AB3PB specimen i.e.:

- involves a simple 3-point bending set-up;

- generates regions of nearly constant bondline shear stress;

- the load-displacement response is quite sensitive to the adhesive shear strength;

- enables the measurement of strength values unaffected by joint end effects.

However, some drawbacks can be pointed out:

- specimen geometry has to be selected taking into account the bondline thickness and shear properties that are not known a priori;

- thick high strength steel adherends will usually be needed to avoid premature adherend yielding;

- owing to the relatively high specimen stiffness, the initial part of the load-displacement curve has low sensitivity to the adhesive shear modulus;

- though facilitated by the present advances in modelling and in obtaining initial parameter estimates, data reduction requires an inverse method;

- bondline shear strain measurements may be affected by difficulties similar to those already reported in other tests.

Experimental studies are underway to assess the actual potential of the AB3PB specimen.

Appendix

As mentioned in Section 2.2, owing to the similarity with [10], the detailed derivation of the present model equations is not done in this paper. Nonetheless, the boundary and continuity conditions leading to Eqs. (11)-(29) are outlined in the next paragraphs. The main $\tau_a(x)$, $\gamma_a(x)$, $N(x)$, $M(x)$ and $v_b(x)$ equations obtained as described in Section 2.2 for the elastic and plastic regions within $0 \leq x \leq L$ (Figs. 1 and 5) do involve integration constants that have to be determined. One must also consider similar equations for the $-c \leq x \leq 0$ overhang (Fig. 1) [10]. The number of integration constants, and thus the number of conditions, varies according to the spread of the adhesive yielding zone. Nevertheless, some conditions always apply i.e.:

- $\tau_a(L) = 0$ and $(dv_b/dx)_{x=L} = 0$, given the symmetry relative to $x = L$ (Fig. 1);

- $v_b(0) = 0$, because of the left support;

- continuity of τ_a, γ_a, N, M, dv_b/dx at $x = 0$, accounting for the constraints imposed by the overhang.

In the fully elastic bondline stage, only the compatibility of $\{\gamma_a(L) - \gamma_a(0)\}$ with Eq. (7) is needed to arrive at Eqs. (13), (17)-(20).

Additional conditions have to be imposed when a plastic region develops (Figs. 1 and 5) i.e.:

- $\tau_a(d) = \tau_{ua}$;

- continuity of N, M, dv_b/dx and v_b at $x = d$;

- compatibility of $\{\gamma_a(L) - \gamma_a(d)\}$ with Eq. (7).

A similar set of conditions is also needed at $x = a$ when the plastic zone has not yet reached the overhang. This leads to Eqs. (11), (12), which provide the limit coordinates of the plastic region, and subsequently to Eqs. (22)-(27). Once the overhang bondline

becomes partially plastic, one must determine first the corresponding limit coordinate e (Fig. 5) by imposing $\tau_a(e) = \tau_{ua}$ and continuity of γ_a, N and M, which results in Eqs. (14)-(16).Finally, compatibility with the main $0 \leq x \leq L$ region yields Eqs. (28) and (29).

References

[1]   da Silva LFM, das Neves PJC, Adams RD, Spelt JK. Analytical models of adhesively bonded joints—Part I: Literature survey. Int J Adhes Adhes 2009;29:319-30.

[2]   He X. A review of finite element analysis of adhesively bonded joints. Int J Adhes Adhes 2011;31:248-64.

[3]   da Silva LFM. Failure strength tests. In: da Silva LFM, Öchsner A, Adams RD, editors. Handbook of adhesion technology, Berlin Heidelberg: Springer-Verlag; 2011, p. 443-71.

[4]   Sutton MA, Orteu JJ, Schreier HW. Image correlation for shape, motion and deformation measurements, New York: Springer; 2009.

[5]   Kosmann J, Klapp O, Holzhüter D, Schollerer MJ, Fiedler A, Nagel C, Hühne C. Measurement of epoxy film adhesive properties in torsion and tension using tubular butt joints. Int J Adhes Adhes 2018;83:50-8.

[6]   Kosmann J, Völkerink O, Schollerer MJ, Holzhüter D, Hühne C. Digital image correlation strain measurement of thick adherend shear test specimen joined with an epoxy film adhesive. Int J Adhes Adhes 2019;90:32-7.

[7]   da Silva LFM, da Silva RAM, Chousal JAG, Pinto AMG. Alternative methods to measure the adhesive shear displacement in the thick adherend shear test. J Adhes Sci Technol 2008;22:15-29.

[8]   Kadioglu F, Vaughn LF, Guild FJ, Adams RD. Use of the thick adherend shear test for shear stress-strain measurements of stiff and flexible adhesives. J Adhes 2002;78:355-81.

[9]   Dragoni E, Brinson HF. Modeling and optimization of the sandwich beam specimen in three-point bending for adhesive bond characterization. Int J Adhes Adhes2016;68:380-8.

[10]   de Morais AB. Analysis of the adhesively bonded three-point bending specimen for evaluation of adhesive shear behaviour. Int J Adhes Adhes 2017;74:40-8.

[11]   Hua Y, Kasavajhala ARM, Gu L. Elastic-plastic analysis and strength evaluation of adhesive joints

in wind turbine blades. Compos Part B 2013;44:650-6.

[12] Albiez M, Vallée T, Fricke H, Ummenhofer T. Adhesively bonded steel tubes - Part I: Experimental investigations. Int J Adhes Adhes 2019;90:199-210.

[13] Chai, H. Deformation and failure of adhesive bonds under shear loading. J Mater Sci 1993;28:4944-56.

[14] Chai H. The effects of bond thickness, rate and temperature on the deformation and fracture of structural adhesives under shear loading. Int J Fract 2004;130:497-515.

[15] Tomblin J, Yang C, Harter P. Investigation of thick bondline adhesive joints. DOT/FAA/AR-01/33. Washington, DC: U.S. Department of Transportation, Federal Aviation Administration, Office of Aviation Research and Development; 2001.

[16] Papakonstantinou JM, Tapia RA. Origin and evolution of the secant method in one dimension. Amer Math Monthly 2013;120:500-18.

[17] Tomblin J, Seneviratne W, Escobar P, Yoon-Khian Y. Shear stress-strain data for structural adhesives. Report No. DOT/FAA/AR-02/97. Washington, DC: U.S. Department of Transportation, Federal Aviation Administration, Office of Aviation Research and Development; 2002.

[18] Burst B, Adams DO. Investigating the thin-film versus bulk material properties of structural adhesives. Report No. DOT/FAA/AR-06/45, U.S. Department of Transportation, Federal Aviation Administration, Office of Aviation Research and Development, Washington, DC, 2008.

[19] Smith WF. Structure and properties of engineering alloys. USA: McGraw-Hill; 1993.

[20] He Y, Makeev A, Shonkwiler B. Characterization of nonlinear shear properties for composite materials using digital image correlation and finite element analysis. Compos Sci Technol 2012;73:64-71.

ELSEVIER SCIENCE
MANUSCRIPT ACCEPTANCE FORM

(to be filled in by the corresponding author and returned to the editor with the finally accepted electronic version of the manuscript)

───

─

Name of Journal: INTERNATIONAL JOURNAL OF ADHESION AND ADHESIVES

───

─
                                                                          Ref:
J1653

Title: A thick bondline beam model for the adhesively bonded 3-point bending specimen

by   Alfredo B. de Morais

Corresponding author's name: Alfredo B. de Morais

Please ensure that the following information is supplied for the corresponding author:

☒   E-mail address   abm@ua.pt

☒   Full postal address

University of Aveiro, Department of Mechanical Engineering, RISCO research unit, Campus Santiago, 3810-193 Aveiro, Portugal

☒   Telephone and fax numberTel.: +351 234 370830; fax: +351 234 370953

Checklist:

☒   Are the keywords supplied?
☒   Are all figures supplied with captions?
☒   Are all tables supplied, and with captions?
☒   Are copyright permission letters enclosed for any artwork/tables previously published, including those published on the world-wide-web?

No copyright permission letters needed.

If any of the illustrations are to be printed in colour please indicate this below: note that in the printed paper, colour costs you about 300 Euros per Fig, while on-line, colour is free

The paper does not contain any colour illustrations.